JGR Space Physics

RESEARCH ARTICLE
10.1029/2020JA028507

GNSS TEC-Based Detection and Analysis of Acoustic-Gravity Waves From the 2012 Sumatra Double Earthquake Sequence

Sarthak Srivastava[1], Amal Chandran[1], Fabio Manta[2], and Benoit Taisne[3]

[1]Satellite Research Centre, Nanyang Technological University, Singapore, Singapore, [2]Institut de Physique du Globe de Paris, CNRS, Paris, France, [3]Earth Observatory of Singapore, Nanyang Technological University, Singapore, Singapore

Key Points:

- Acoustic-gravity waves from the 2012 Sumatra double earthquake sequence were detected in GNSS data and sources were traced using a geometric model
- Presence of acoustic resonant frequencies and wave speeds below 2 km/s suggests coseismic ground movement as the wave generation mechanism
- Directivity in wave propagation is explained by the orientation of geomagnetic field using a simple model

Correspondence to:
A. Chandran,
achandran@ntu.edu.sg

Citation:
Srivastava, S., Chandran, A., Manta, F., & Taisne, B. (2021). GNSS TEC-based detection and analysis of acoustic-gravity waves from the 2012 Sumatra double earthquake sequence. *Journal of Geophysical Research: Space Physics*, *126*, e2020JA028507. https://doi.org/10.1029/2020JA028507

Received 21 JUL 2020
Accepted 15 MAY 2021

Abstract The Wharton Basin earthquake sequence on April 11, 2012, offshore Sumatra, represents the two largest ($M_w > 8.0$) strike-slip earthquakes ever recorded. Ground fault displacements generated a spectrum of acoustic-gravity waves due to solid Earth–atmosphere coupling. Wave-like perturbations in Total Electron Content (TEC) were therefore observed in ground-based Global Positioning System data. The waves arrive about 10 min after each earthquake and their spectral analysis reveals the presence of acoustic resonance frequencies of 3.8 and 4.4 mHz. The acoustic wave speeds of 0.9–1.2 km/s suggest coseismic ground movement as the primary wave generating mechanism instead of seismic Rayleigh waves. Gravity waves with frequencies below 2 mHz traveling with lower speeds of 0.21 km/s are also detected. Ray tracing using a simple numerical model traced the source of observed ionospheric perturbations to within 150 km distance of the epicenters. Large amplitude ionospheric disturbances were found to travel mostly in a north-south direction, an observation explained by the orientation of Earth's geomagnetic field.

1. Introduction

1.1. Acoustic-Gravity Waves From Earthquakes

Ionospheric disturbances following seismic events arising due to surface–atmosphere coupling have been studied previously (Calais & Minster, 1995; K. Davies & Baker, 1965). Earthquakes result in vertical and horizontal ground displacement. Normal and reverse thrust fault earthquakes result in mostly vertical while strike-slip faults result in mostly horizontal displacement. These ground movements can induce acoustic-gravity waves in the atmosphere (Rolland, Lognonné, & Munekane, 2011; Rolland, Occhipinti, et al., 2010). Waves originating from the source region first propagate obliquely upward and then spread horizontally as acoustic-gravity waves (Mikumo & Watada, 2010).

There are four different pathways for atmospheric wave generation due to earthquakes (Mikumo & Watada, 2010; Occhipinti, 2016; ReVelle, 2008). The first is low-frequency (less than Brunt–Väisälä frequency) gravity waves generated at the source and propagating upward to long distances (Afraimovich, Perevalova, et al., 2001). The second one is higher-frequency infrasonic or acoustic waves (higher than acoustic cutoff frequency) also generated at the source (Bolt, 1964). These infrasonic waves can get reflected or diffracted due to topography (Young & Greene, 1982) or sound velocity variations (Drob, Picone, & Garcés, 2003) during propagation. The third case is also infrasonic waves but generated due to coupling of atmosphere with seismic Rayleigh waves along the ground surface (Donn & Posmentier, 1964). Coupling of the atmosphere with Rayleigh surface waves is found to be most effective at frequency ~3.7 mHz. Ionospheric disturbances corresponding to Rayleigh waves travel at ~3–4.5 km/s, much higher than direct acoustic waves from the source (~1 km/s at 400 km altitude) (Ducic et al., 2003; Heki & Ping, 2005). Thus, two kinds of acoustic infrasonic waves are generated by earthquakes (Le Pichon et al., 2002). Some simulations (Artru et al., 2005) suggest that trapping of acoustic waves with periods between 4 and 6 min can occur in lower atmosphere. The fourth case is generation of gravity waves by ocean tsunami waves that are themselves generated from large earthquakes. These waves occur due to coupling of the atmosphere with ocean surface displacement and are detected in the ionosphere a few hours after the earthquake (Artru et al., 2005; Occhipinti, Lognonné, et al., 2006) as opposed to ~10 min for waves due to seismic Rayleigh origin.

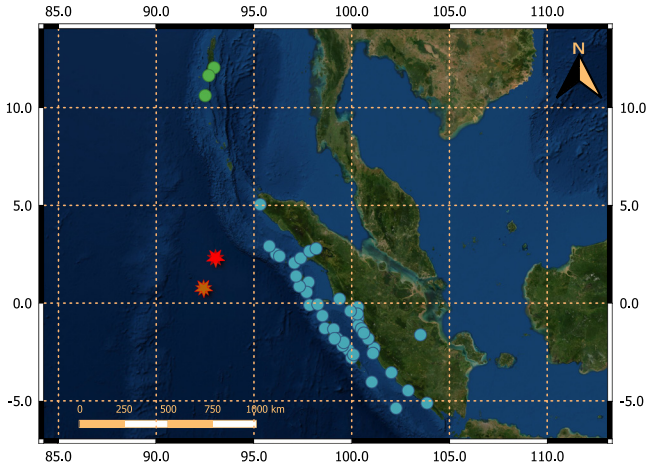

Figure 1. Map showing the location of earthquake epicenters (the red marker represents the epicenter of quake 1 and the orange marker represents the epicenter of quake 2). The Sumatra GPS Array (SuGAr) stations are blue circles; International GNSS (Global Navigation Satellite System) Service (IGS) stations are green circles.

The restoring mechanism for gravity waves is buoyancy force while for acoustic waves the pressure gradient force provides the restoring mechanism. As the waves propagate upward, their amplitude increases due to decreasing density, obeying conservation of kinetic energy. The extent of upward propagation of waves depends on their launch angle. Upon encountering a purely vertically varying horizontal background flow, gravity waves can undergo either reflection (turning point) or critical-level filtering (C. J. Heale & Snively, 2015). Reflection occurs when the wave is against the wind direction, resulting in Doppler shifting of intrinsic frequency toward the buoyancy frequency and the vertical wavelength approaching infinity. If two turning points are present at different altitudes, the wave can get ducted and propagate horizontally. Ducted waves can deposit energy in regions far away from the source (C. Heale et al., 2014; Suzuki, Shiokawa, et al., 2013, Suzuki, Vadas, et al., 2013; Yu & Hickey, 2007). Critical-level filtering occurs when the wave propagates in the wind direction and the phase speed approaches mean wind speed such that the intrinsic frequency approaches zero. While the horizontal wavelength remains constant, vertical wavelength then tends to zero.

Heki and Ping (2005) performed simulations to show that only waves launched with zenith angles between 0° and 20° can propagate to ionospheric heights and cause fluctuations in electron density. For other zenith angles, waves get reflected primarily due to atmospheric vertical temperature profile. Horizontal propagation in the ionospheric region depends on the direction of local geomagnetic field since the ions couple with the field owing to small normalized ion-neutral collision frequency (J. A. Davies et al., 1997; Heki & Ping, 2005).

Atmospheric waves reaching ionospheric heights can perturb the electron density which can be detected in Global Navigation Satellite System (GNSS) signal differential delay, as evidenced by several studies. Acoustic-gravity waves associated with thunderstorms have been detected in Global Positioning System (GPS) Total Electron Content (TEC) data by Lay et al. (2015). Azeem and Barlage (2018) detected convectively generated concentric gravity waves as Traveling Ionospheric Disturbances from GPS TEC data. Several studies have used GPS-derived electron content data to analyze earthquake-generated acoustic-gravity waves (Astafyeva & Heki, 2009; Calais & Minster, 1995; Heki & Ping, 2005; Mikumo & Watada, 2010; Rolland, Lognonné, Astafyeva, et al., 2011; Rolland, Lognonné, & Munekane, 2011; Saito et al., 2011). Manta et al. (2020) have demonstrated quick evaluation of tsunamigenic potential of earthquakes using GPS TEC.

1.2. The 2012 Sumatra Earthquake

The 2012 Wharton Basin great earthquake sequence consisted of the two largest (Moment magnitude (M_w) > 8.0) strike-slip earthquakes ever recorded, occurring within a span of 2 h on April 11, 2012 (day of the year DOY 102). The Moment magnitude (M_w) is a logarithmic scale measure of an earthquake's magnitude based on its seismic moment. Unlike other seismic magnitude scales, the Moment magnitude scale can characterize large earthquakes accurately (Hanks & Kanamori, 1979). The first $\boldsymbol{M_w}$ 8.6 earthquake (henceforth referred to as quake 1) occurred off the western Sumatra coast at 08:38:37 UTC with coordinates 2.32°N, 93.06°E as reported by the US Geological Survey. The second earthquake (quake 2) happened at 10:43:09 UTC approximately 200 km south at 0.77°N, 92.45°E with an intensity of $\boldsymbol{M_w}$ 8.2 (Duputel et al., 2012). Quake 1 happens to be the largest strike-slip earthquake in an interplate region (Yadav et al., 2013). The main shock (quake 1) happened with multiple ruptures (Hill et al., 2015) and the aftershock (quake 2) had a bilateral rupture fault (Yue et al., 2012). The earthquakes were largely strike-slip dominated with slip as large as 30 m (Yadav et al., 2013). Coseismic ionospheric disturbances caused by strike-slip earthquakes are not well studied owing to their infrequent occurrence (Astafyeva & Heki, 2009). Thus, this double earthquake sequence provides an opportunity to study atmospheric waves induced by strike-slip-dominated large earthquakes. Figure 1 shows the epicenters of the earthquake sequence along

with the locations of GPS stations used in this study. Most stations of the Sumatra GPS Array (SuGAr) are located very close to each other, providing an opportunity to explore the event with a high spatial resolution.

2. Data and Methods

2.1. TEC Derivation From GPS Data

Differential delay between GPS phase observables φ_1 and φ_2 corresponding to the GPS carrier frequencies $f_1 = 1{,}575.42$ MHz and $f_2 = 1{,}227.6$ MHz is proportional to the integrated electron number density along signal propagation path, called TEC. TEC can be computed using

$$\mathbf{TEC} = \left[\varphi_2 - \frac{f_2}{f_1}\varphi_1 + n + f_2\left(b_r + b_s \right) \right] \frac{f_1^2 f_2}{f_1^2 - f_2^2} \frac{c}{A} \tag{1}$$

where $A = 40.3\ \mathbf{m}^3\ \mathbf{s}^{-2}$ and c is the speed of light, b_r and b_s are code delay biases specific to the receiver and satellite hardware, respectively, and n is a constant for each orbital arc caused by phase ambiguities. TEC is measured in TEC Units (TECU) with 1 TECU $= 10^{16}$ **el** / $\mathbf{m}^2$. Line-of-sight TEC (also called Slant TEC or STEC) computation from raw GPS data is detailed in Dautermann et al. (2009) and Mannucci et al. (1999). The STEC is then transformed into vertical TEC (VTEC) using a suitable mapping function $M(\varepsilon)$ following

$$\mathrm{VTEC} = \frac{\mathrm{STEC}}{M(\varepsilon)} \tag{2}$$

Different mapping functions are described and compared in Meggs et al. (2004) and Zhong et al. (2016). VTEC values thus obtained correspond to the vertically integrated electron content over the subionospheric pierce points (SIPs). SIPs are locations on ground below the point where satellite-receiver line of sight intersects the ionosphere (assumed to be a thin shell at 350 km altitude).

2.2. GPS TEC Data Analysis

The SuGAr is a network of 49 ground-based GPS stations along the convergent plate boundary between Indo-Australian and Asian tectonic plates in western Sumatra, Indonesia (McLoughlin et al., 2011). Data from SuGAr have previously been used to study earthquakes and plate-tectonics in south-east Asia (Ammon et al., 2005; Gahalaut & Catherine, 2006; Subarya et al., 2006) as well as ionospheric signature of earthquakes (Manta et al., 2020).

We used data from 41 SuGAr and 3 additional IGS (International GNSS Service) stations and each station-satellite VTEC time series was considered separately for analysis. Data for period 08:30–12:00 UTC, April 11, 2012, is considered. A temporal availability constraint of 60% is imposed. Station-satellite pairs with coverage less than this availability constraint are not considered. A minimum elevation constraint of 10° is further imposed as slant-to-vertical TEC conversion error is proportional to path length which is longer for lower elevation angles. It was found that any discontinuities in satellite visibility from a station lead to jumps in TEC values which can provide a false signal of wave presence. Upon removal of such discontinuities, the VTEC time series for each station-satellite pair is ready for analysis.

First, longer duration trends in VTEC are removed. For filtering of VTEC data, a zero-phase fourth-order Butterworth filter with passband 0.9–5.6 mHz (or 3–18 min periods) was employed on the detrended perturbations to solely retain the frequencies corresponding to acoustic and gravity waves (Astafyeva et al., 2014; Rolland, Lognonné, & Munekane, 2011). Note that given 15s cadence of GPS data, waves with a maximum of 16 mHz (half the Nyquist frequency) are detectable (Dautermann et al., 2009). Figure 2 shows some examples of filtered VTEC data for four such station-satellite pairs. Low elevation IPPs could exhibit multipath and there could be false peaks in perturbation simply due to spatial variations due to moving IPPs. We visually inspect VTEC time series that are continuous, free from erratic noise, and only use the inspected data for further analysis. We only observe clear spikes in filtered TECs consistently from 5 to 6 satellites out of 32 GPS satellites, due to varying factors such as limited coverage or low elevation or too far range (Artru et al., 2005).

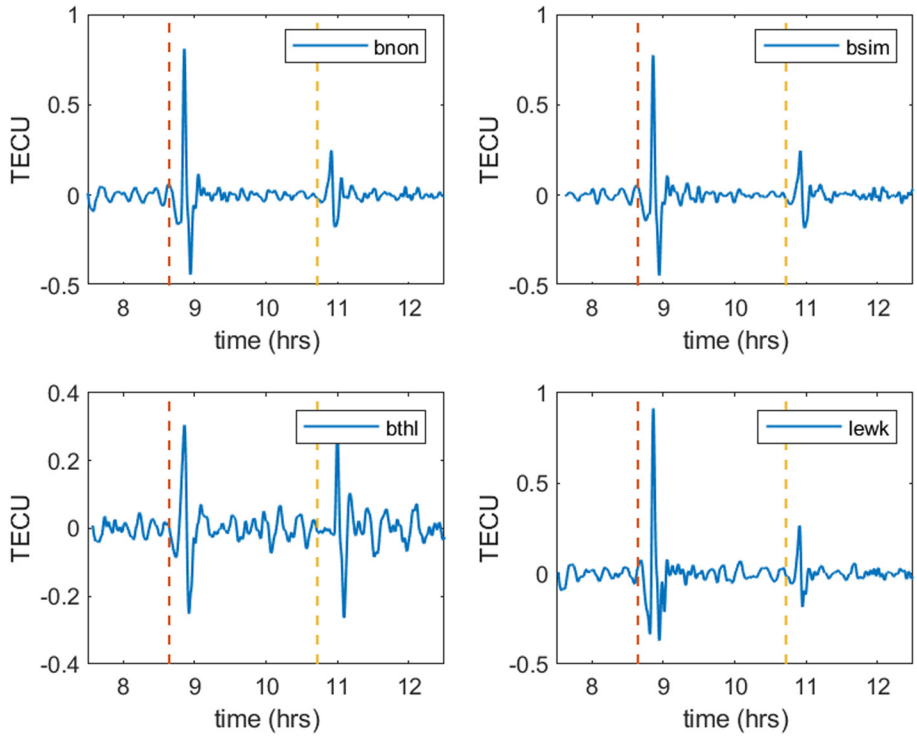

Figure 2. Filtered Total Electron Content (TEC) time series observations extracted from four different GNSS stations with respect to satellite 32. Clear perturbations of the ionospheric TEC are visible 10–15 min after the two earthquake events (dashed lines).

2.3. Geomagnetic Conditions

Since geomagnetic variability can have a significant impact on GPS-derived TEC (Afraimovich & Astafyeva, 2008; Warnant & Pottiaux, 2000), it is important to check the geomagnetic activity level for the analysis period.

Figure 3 shows the planetary 3-h range Kp index for DOY 101 to 103 obtained from World Data Center for Geomagnetism, Kyoto (http://wdc.kugi.kyotou.ac.jp/kp/index.htm). The Kp values for the analysis day (shaded orange) are 2 or less, corresponding to a relatively low geomagnetic activity (Chang et al., 2011; Nayak & Yiğit, 2018).

To further confirm the stability of the geomagnetic field, we analyzed the disturbance storm time (Dst) index for entire month of April (WDC Kyoto Observatory; http://wdc.kugi.kyoto-u.ac.jp/dstprovisional/index.html) (Figure 4). The Dst index shows values close to zero suggesting absence of any significant geomagnetic storms at the time of the 2012 Sumatra double earthquake sequence (McPherron & O'Brien, 2001). This provides confidence that the perturbations in GPS TEC are due to atmospheric drivers and not from geomagnetic variabilities.

2.4. Acoustic-Gravity Wave Domains

The mean vertical neutral temperature profile of the atmosphere is obtained from the NRLMSISE-00 model (Picone et al., 2002) for April 11, 2012 10:00:00 UTC at coordinates (0°, 95°). The F10.7 daily average index is 93.7 and the daily ap index is 4.5. Based on the temperature profile, we obtain the Brunt–Väisälä (ω_{BV}) and acoustic cutoff (ω_a) frequencies using:

$$\omega_{BV} = \frac{(\gamma - 1)^{0.5} g}{c_s} \tag{3}$$

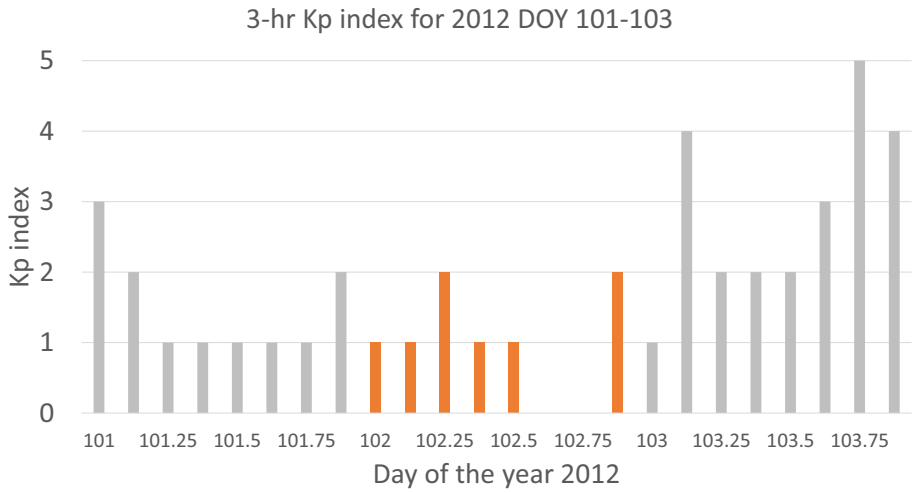

Figure 3. Three-hour range Kp index of period from the day before the event day of the year (DOY 101) to the day after the event (DOY 103). In orange are highlighted the measurements on the day of the two earthquakes DOY 102 (April 11, 2012).

$$\omega_a = \frac{\gamma g}{2c_s} \tag{4}$$

where γ is the specific heat ratio and c_s is the speed of sound. Figure 5 shows the calculated frequencies. In general, $\frac{\omega_a}{2\pi} = 3.3$ mHz and $\frac{\omega_{BV}}{2\pi} = 2.9$ mHz at lower altitudes. Waves with frequencies lying between ω_a and ω_{BV} are evanescent and cannot propagate (Jones & Bedard, 2018).

3. Results and Discussion

3.1. Wave Characterization

Wave propagation is shown in hodochrone for different satellite-receiver pairs in Figure 6. The hodochrone is a true distance–time diagram constructed by taking into account the time-varying geographical location of individual SIPs. We plot contours of VTEC at SIPs on distance from epicenter versus time axes to obtain the hodochrones. Figure 6 shows clearly propagating waves starting ~10 min after both quakes. The slope of the outward traveling disturbances can provide an estimate of the wave speeds. The hodochrones suggest wave speeds ~0.9–1.2 km/s for both the quakes which corresponds to typical acoustic wave speeds at ionospheric heights (Yeh & Liu, 1974). Ionospheric disturbances traveling at acoustic speeds have been observed in other GPS TEC detections of gravity waves borne out of seismic activity (Astafyeva & Heki, 2009; Occhipinti, Rolland, et al., 2013; Rolland, Lognonné, & Munekane, 2011). Acoustic wave signature in quake 1 (M_w

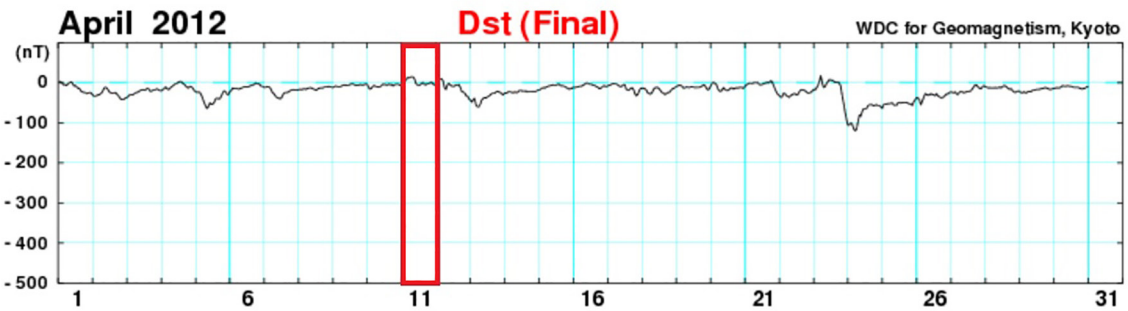

Figure 4. Disturbance storm time (Dst) storm index for the month of April 2012. Red box highlights DOY 102 (11 April), which shows a very small Dst value.

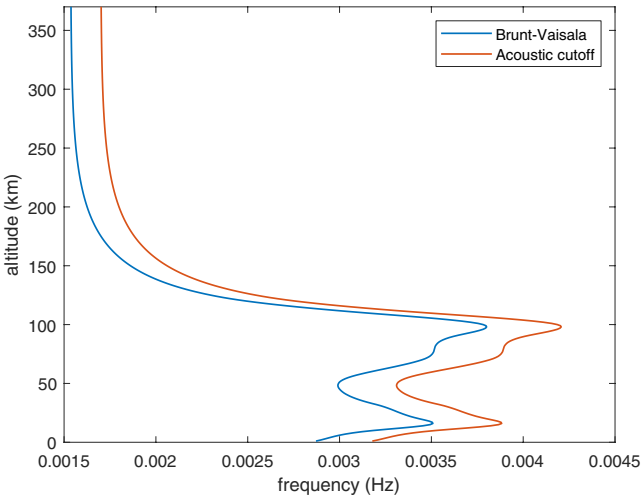

Figure 5. Acoustic cutoff and Brunt–Väisälä frequency profiles estimated from vertical neutral temperature profile obtained from the NRLMSISE-00 model for April 11, 2012 10:00:00 UTC at coordinates (0°, 95°).

8.6) seems to be more intense (darker color) and last for ~30 min which is longer than ~18 min for quake 2 (M_w 8.2).

We also observe much slowly moving structure emanating from quake 1. This structure is only visible in the far-field range, over 1,000 km from the epicenter. Based on reading off the hodochrones, this structure is found to propagate at much slower speeds of ~0.21 km/s which is too slow for acoustic waves at 350 km altitude (Heki & Ping, 2005). This slow-moving structure could be caused by gravity waves. Following Medvedev and Yiğit (2019), the maximum intrinsic horizontal phase speed of gravity waves is given by

$$\hat{c}_{\max} = 2NH$$

where N is the Brunt–Väisälä frequency (in rad/s) and H is the atmospheric scale height. Taking $N \sim 0.0182$ rad/s (i.e., 2.9 mHz) and $H \sim 8.5$ km, we obtain $\hat{c}_{\max} \sim 0.3$ km/s. Using the Horizontal Wind Model-07 (Drob, Emmert, et al., 2008), we find horizontal wind magnitude to be ~0.025 km/s. Thus, ground-based (extrinsic) maximum horizontal phase speed $c_{\max} \approx \hat{c}_{\max} = 0.3$ km/s. This is the maximum propagation speed for gravity waves that can be seen on hodochrones. The speed of the slow-moving structure (0.21 km/s) is lower than the maximum possible horizontal speed of gravity waves. We reproduce the wave travelogram with perturbations band passed between 2 and 5.6 mHz in Figure 7. Acoustic wave signatures from both the quakes are visible but the slow-moving structure is absent. This suggests that the frequency of the slow-moving structure is lower than 2 mHz.

To identify the dominant frequencies in the filtered TEC perturbations, we perform a wavelet analysis of the filtered time series data. Wavelet analysis is a powerful technique that has been used widely in spectral analysis of TEC data and atmospheric science in general (Azeem & Barlage, 2018; Borries et al., 2009; Heki & Ping, 2005; Rolland, Lognonné, & Munekane, 2011). Figure 8 shows an example of wavelet analysis performed with filtered TEC perturbation time series between station LEWK and GPS satellite 32. The time series shows very clear spikes corresponding to the two earthquakes. We employ Morse wavelet to obtain the frequency spectrum. The thick black lines on the wavelet spectrogram identify the cone of influence beyond which the data are unreliable because of significant edge effects. The thin black contours surrounding the

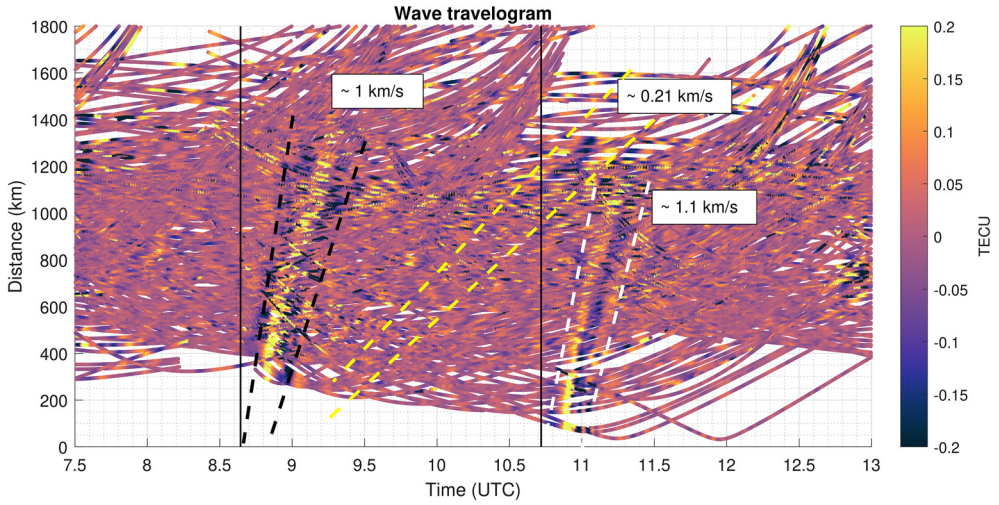

Figure 6. Hodochrone of Vertical Total Electron Content (VTEC) perturbations. Vertical black lines show the onset time for both quakes. Black and white dashed lines show acoustic waves resulting from quake 1 and quake 2, respectively. Yellow dashed lines show another visible structure traveling at much slower speeds, suggesting that they could be signatures of gravity waves.

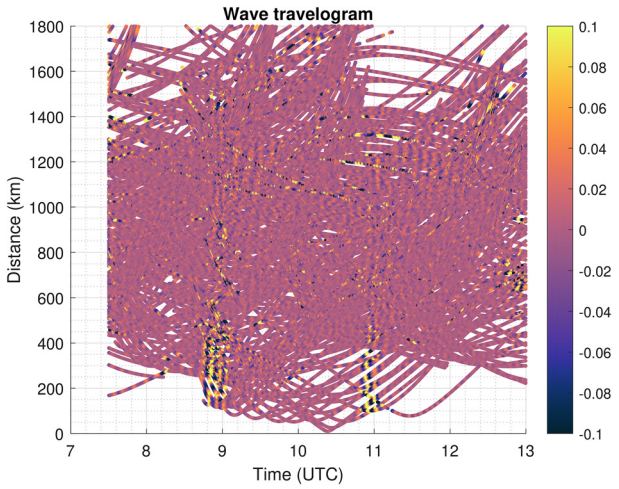

Figure 7. Hodochrone of VTEC perturbations band passed between 2 and 5.6 mHz. Acoustic wave signatures from both the quakes are still visible but the slow-moving (0.21 km/s) structure is absent.

bright spots identify frequencies above 95% confidence level (significance at 5%) based on red-noise spectrum (Torrence & Compo, 1998). Thus, features within the significance contours and within the cone of influence only need be studied. The two dashed horizontal lines correspond to the representative 2.9 mHz Brunt–Väisälä frequency and 3.3 mHz acoustic cutoff frequency, respectively. The vertical dashed lines represent the onset times of the two earthquakes.

We observe time series fluctuations after about 10 min of either quake. Perturbations corresponding to the second quake are noticeably smaller in magnitude, presumably due to lower intensity of quake 2. We observe a range of frequencies in the spectrogram, from as low as 1 mHz gravity waves to as high as 6.5 mHz acoustic waves. We also observe that the gravity waves persist for much longer than the acoustic waves.

We separately plot spectrogram for acoustic waves (frequencies >3.3 mHz) in Figure 9 to look for any acoustic resonance frequencies. In quake 1, we identify a 4.4 mHz peak. Also, a ~3.8 mHz acoustic wave is seen to persist till about 45 min after the quake occurrence. The identified acoustic waves closely match the two fundamental acoustic resonance frequencies of 3.7 and 4.4 mHz calculated by Lognonné et al. (1998) previously. Rolland, Lognonné, Astafyeva, et al. (2011) and Saito et al. (2011)

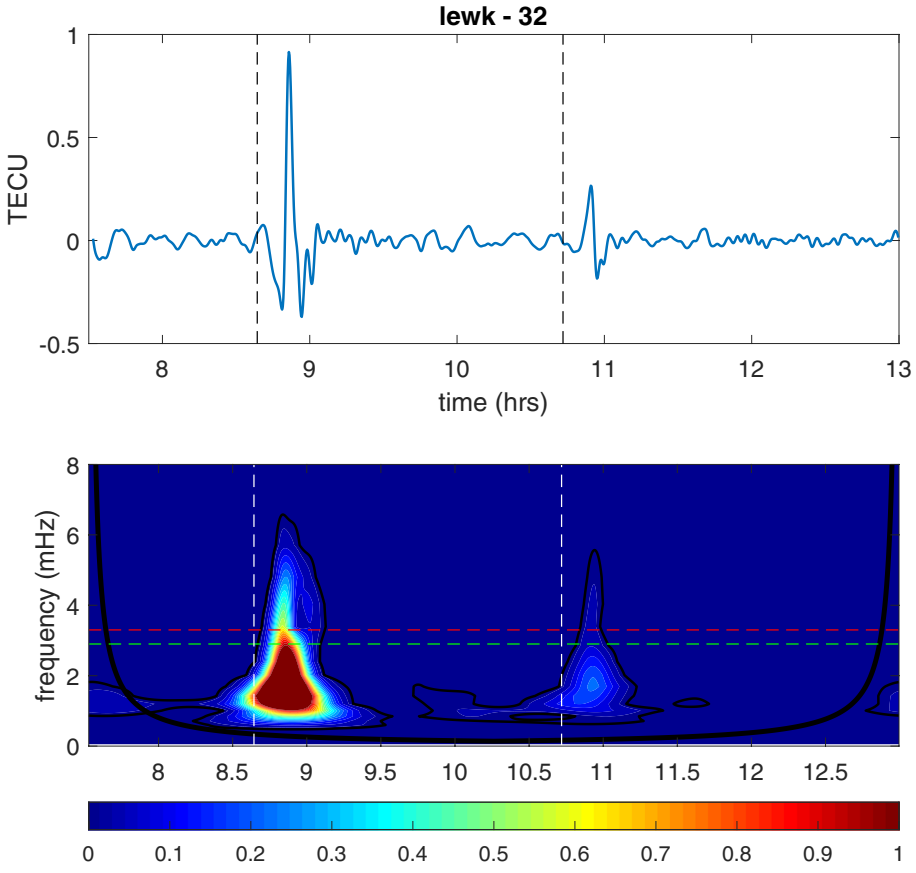

Figure 8. TEC perturbation time series for station LEWK-satellite 32. The corresponding wavelet spectrogram shows the frequencies above red noise significance level. Horizontal red dashed line is the representative acoustic cutoff frequency (3.3 mHz) and green dashed line is the Brunt–Väisälä frequency (2.9 mHz). Vertical white dashed lines correspond to the earthquake times.

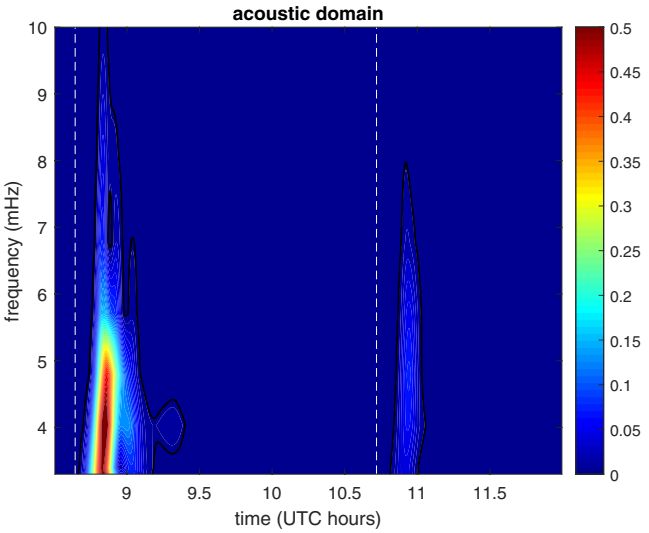

Figure 9. Wavelet spectrogram for LEWK-satellite 32 time series for frequencies over acoustic cutoff frequency (3.3 mHz). Frequencies above red noise significance level are shown. White dashed lines correspond to the earthquake times.

also observed trapped acoustic mode at 3.7 mHz after the 2011 Tohoku Earthquake. Perturbation after quake 2 reveals dominant acoustic frequency corresponding to ~5 mHz. Sunil et al. (2015) have suggested that the 5 mHz frequency observation could be due to the shifting of acoustic resonance mode by F-layer wind velocity. The frequency signatures suggest that the seismic vibrations triggered the acoustic modes in the atmosphere, which propagated to the ionosphere and caused perturbations in the F-layer. These perturbations resulted in delay in GPS signal propagation that was observed as fluctuations in TEC. It is noted that only waves with vertical wavelengths larger than the F-layer thickness or waves consisting mostly of one phase along the slant path can be discovered in the TEC data due to reduced possibility of cancellations of electron amplitudes (Azeem & Barlage, 2018).

3.2. Localization of Wave Sources

Ducic et al. (2003) proposed a two-step mechanism for coseismic ionospheric disturbance propagation: at first, the seismic Rayleigh wave travels along the Earth's surface, followed by atmospheric waves triggered by ground vibrations which then propagate to ionospheric heights. With this mechanism, the speed of observed ionospheric disturbances should correspond to those of Rayleigh waves ~3.8 km/s. However, disturbance propagation speeds observed from hodochrone are much lower and closer to acoustic velocities in the upper atmosphere. This suggests that the acoustic wave generation is likely caused due to coupling of solid Earth's motion with the atmosphere near source region instead of the Rayleigh wave mechanism. The waves first propagate upward and then horizontally at ionospheric heights. In fact, the acoustic wave speeds observed in the hodochrone are slightly faster than sound speeds are expected at ionospheric heights. Heki and Ping (2005) postulate that ionospheric wind could be a reason for this. Heki and Ping (2005) attribute the absence of Rayleigh wave signatures to their lack of coherence to disturb the atmosphere but suggest that they could be detected in TEC time series >2,000 km away from the epicenter as the acoustic waves would have decayed.

We now employ a simple ray tracing technique commonly used in seismology (Aki & Richards, 2002; Lee et al., 1981) to localize the source of the observed waves. First, we obtain the horizontal and vertical propagation speeds by plotting arrival time of maximum TEC amplitude for all the station–satellite pairs. All perturbation time series are visually inspected and only those with significant peak and low noise are shortlisted. Arrival time of peak perturbation is plotted with distance from the epicenter to obtain a linear plot, as shown in Figures 10 and 11.

Following Liu et al. (2006) and Tsai et al. (2011), we use gradient and intercept from the regression line to obtain the wave speeds. A similar method but with the added iteration over propagation speed values was used by Afraimovich, Astafieva, and Kirushkin (2006), Kiryushkin and Afraimovich (2007), Liu et al. (2006), and Tsai et al. (2011). However, their results show that computed speeds by iteration are similar to those obtained from linear regression. Hence, we employ the former method to simplify our simulation. We take the vertical propagation speed V_V as ionospheric height (H_{ion} = 350 km) divided by duration of the first arrival, leading to V_V = 0.34 km/s for quake 1 and 0.52 km/s for quake 2, respectively. The slope provides mean horizontal propagation speed V_H = 1.21 km/s for quake 1 and 0.68 km/s for quake 2, respectively. A 30° latitude × 40° longitude grid with resolution of 0.1° is defined for computation. For each point $\boldsymbol{p}$ on the grid, we compute travel time $\Delta t_{p,s}$ of the waves to each maximum perturbation SIP $\boldsymbol{s}$ using:

$$\Delta t_{p,s} = \frac{H_{ion}}{V_V} + \frac{d_{p,s}}{V_H} \tag{5}$$

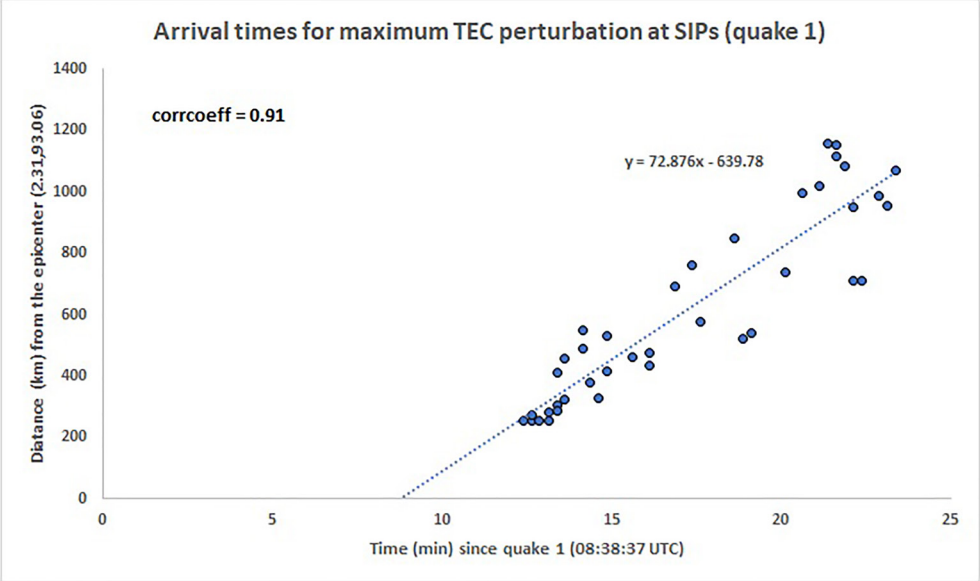

Figure 10. Epicentral distance versus arrival times (since earthquake) of peak TEC disturbances for quake 1.

where $d_{p,s}$ is the great arc distance between each grid point and maximum perturbation SIP. By subtracting the travel time thus computed from the actual recorded time corresponding to maximum amplitude $t_{\max,s}$, we obtain the computed onset times for each grid point:

$$t_{\text{computed},p-s} = t_{\max,s} - \Delta t_{p,s} \tag{6}$$

This process is repeated for all the maximum perturbation SIPs resulting in 120,701 computations per grid made 39 times corresponding to the number of maximum perturbation SIPs ($N = 39$) in quake 1 and again

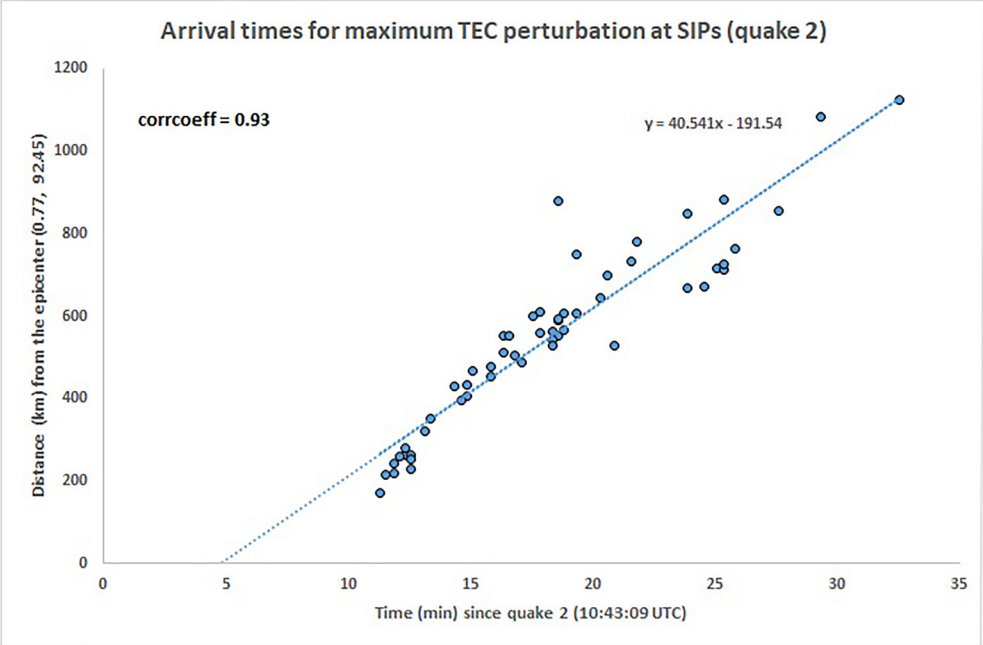

Figure 11. Epicentral distance versus arrival times (since earthquake) of peak TEC disturbances for quake 2.

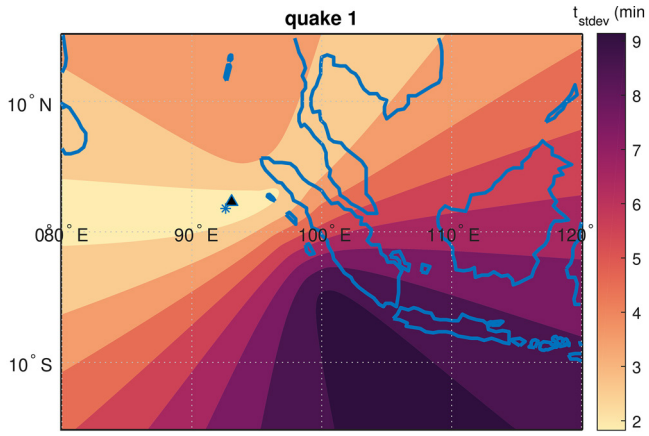

Figure 12. Ray tracing result for quake 1 showing contours of standard deviation (minutes) in arrival time estimation for different grid points. Asterisk shows the minimum standard deviation point, corresponding to the estimated wave source. Solid triangle is the reported epicenter.

55 times for the number of maximum perturbation SIPs in case of quake 2 ($N = 55$). We compute the standard deviation for computed travel times for each grid point using:

$$\sigma_p = \sqrt{\frac{\Sigma\left(t_{\text{computed},p-s} - \mu\right)}{N}} \tag{7}$$

where μ is the mean value for the grid point p. Contour plots of the standard deviation of computed onset times are shown in Figures 12 and 13.

The grid point corresponding to the minimum standard deviation in the contour plots is the wave source traced by the model. Our model predicts (1.8°N, 92.6°E) source coordinates for quake 1: within 76.5 km of the reported epicenter and (0.8°N, 91.3°E) source coordinates for quake 2: within 128 km of the reported epicenter. The ray-traced source coordinates are shown as asterisks in Figures 12 and 13, and they can be seen to be very close to the epicenters (black triangles). This simple ray tracing approach is effective in localizing the wave source and the results demonstrate that the observed waves are indeed seeded by the earthquake sequence.

3.3. Directivity

Previous studies (Astafyeva, 2019; Calais et al., 1998; Heki & Ping, 2005; Rolland, Vergnolle, et al., 2013; Sunil et al., 2015) have indicated that interaction of local geomagnetic field is a likely cause of directional bias in propagation of ionospheric disturbances. The ratio of ion-neutral collision frequency and ion gyro-frequency is small at F-layer heights (J. A. Davies et al., 1997; Heki & Ping, 2005). Thus, ions are coupled to the geomagnetic field and do not move with the neutral particles. Ions moving perpendicular to the field will experience Lorentz force that will hamper their movement. Acoustic waves, being longitudinal, would thus not propagate if their wavefronts are parallel to the field.

To ensure that any observed directivity in wave propagation is not a result of observational bias, we create an azimuthal plot of the number of SIPs for both the quakes. The plots in Figure 14 show the number of SIPs within 30 min of either quakes in 15° azimuth bins. We observe adequate coverage of VTEC data across all azimuth angles.

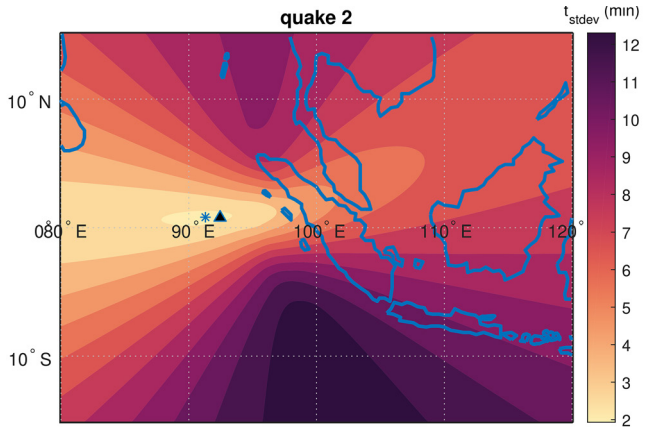

Figure 13. Ray tracing result for quake 2 showing contours of standard deviation (minutes) in arrival time estimation for different grid points. Asterisk shows the minimum standard deviation point, corresponding to the estimated wave source. Solid triangle is the reported epicenter.

To estimate the directions of preferential propagation, we compute the angle between acoustic wave vectors and local magnetic field. We define wave vectors for all azimuths from epicenters to points on a latitude–longitude grid at 350 km height. We compute the local magnetic field vector at each grid point using the International Geomagnetic Reference Field model. Use of three-dimensional magnetic field vector accounts for both magnetic inclination and declination effects. Angular difference is then calculated between these two vectors defined in North-East-Down frame. When the angular difference between wave vector and local magnetic field is small, acoustic wavefronts are more perpendicular to the magnetic field and the ions move along the magnetic field. The wave should propagate in this case. When the wave vector is not aligned with magnetic field vector, the reverse is true and the wave should not propagate because of Lorentz force hampering the ion motion (Rolland, Lognonné, & Munekane, 2011; Sunil et al., 2015).

Contours of angular difference between wave vectors and magnetic field are plotted in Figure 15 for both the quakes. The contours are overlaid with SIPs with only significant amplitudes (perturbation amplitude >0.1 TECU). By displaying only significant amplitudes, we can identify directions along which ionospheric perturbations tend to propagate

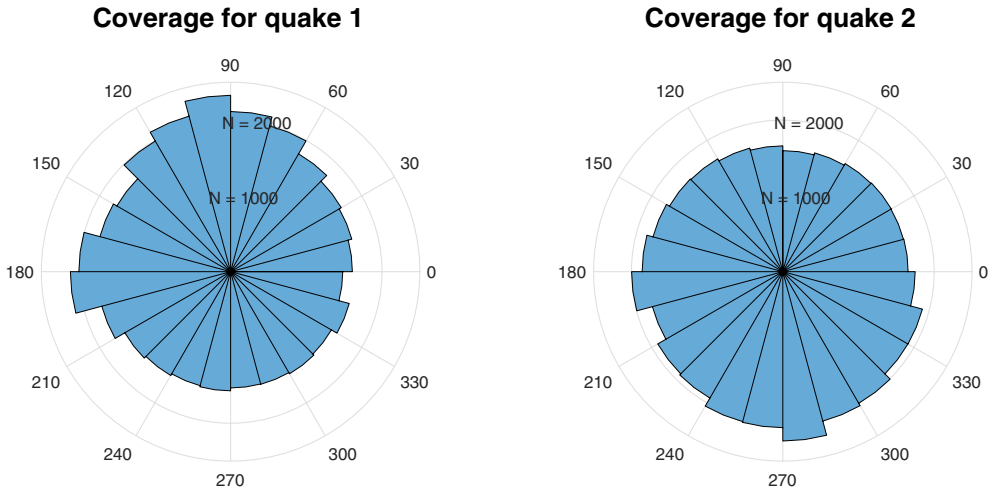

Figure 14. Number of subionospheric pierce points (SIPs) *N* within 30 min of both the quakes plotted against the corresponding azimuth angles. The well-rounded plots indicate that SIPs across all azimuth angles have been observed.

preferentially. Most of the large amplitude SIPs are found in regions where wave vector is nearly parallel or antiparallel to the local magnetic field. These observations follow the preferential propagation mechanism based on geomagnetic field explained earlier. Another observation is made that high amplitude disturbances travel further northward than southward, corroborating findings of Sunil et al. (2015).

4. Conclusion

Acoustic-gravity waves generating from the 2012 Sumatran double earthquake sequence were identified using GPS electron content data. Wave signatures corresponding to acoustic resonant frequencies 3.8 and 4.4 mHz were found indicating coupling between solid Earth and the atmosphere. Gravity waves with frequencies lower than 2 mHz were also found, suggesting generation of a spectrum of waves from the earthquakes. The observed wave speeds were below 2 km/s and significantly lower than Rayleigh wave speeds,

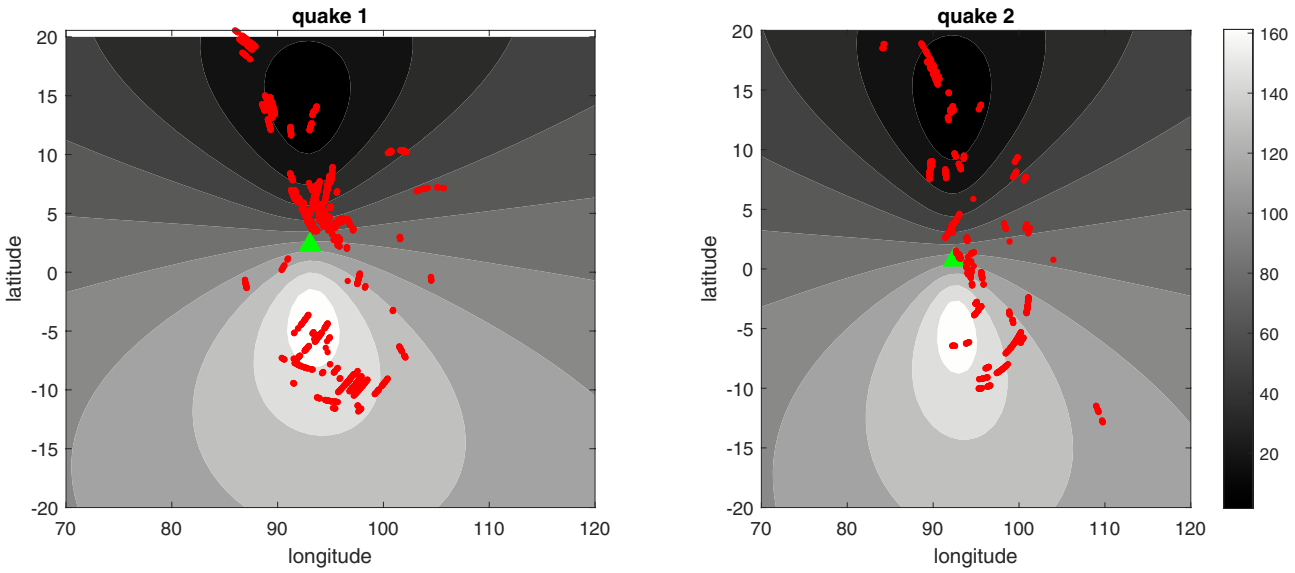

Figure 15. Contours plot of wave directivity based on geomagnetic field. Red dots representing subionospheric pierce points (SIPs) with amplitude >0.1 TECU are overlaid on contours of angular difference between wave vectors and local magnetic field. Most high amplitude SIPs are seen to fall in regions where wave fronts are nearly perpendicular to the local magnetic field. Green triangles locate the epicenter of the earthquakes.

thus ruling out seismic Rayleigh waves as the trigger for atmospheric waves. TEC wave signature for quake 1 was found to be more intense and longer in duration than for quake 2, indicating the difference in intensity of both earthquakes. Wave speeds being closer to acoustic wave speeds at ionospheric heights suggest generation of atmospheric waves by coseismic ground movement instead.

Unambiguous double peak wave signatures corresponding to the double earthquake sequence as well as quieter geomagnetic conditions strongly link the observed waves to the earthquake sources. Furthermore, source tracing using a simple geometric method traced the quake epicenters to within 150 km accuracy. Large number of closely located GPS stations enabled observation of directivity in propagation of perturbations. This directivity was explained by interaction of moving ions with the local geomagnetic field using a simple model. The effect of sea depth needs to be considered to calculate the precise acoustic modes for these submarine earthquakes. The effect of ionospheric winds on shifting the observed frequency for the second quake also needs explaining for fully understanding the generation of ionospheric disturbances caused by these earthquakes through acoustic-gravity waves.

Data Availability Statement

The data files associated with results presented in this paper are available at the Data Repository, NTU at https://doi.org/10.21979/N9/SKQRTF.

Acknowledgments
The authors are grateful to Dr Emma M. Hill of the Asian School of Environment, NTU Singapore for her invaluable assistance in providing the SuGAr GPS data and feedback on the manuscript.

References

Afraimovich, E. L., & Astafyeva, E. I. (2008). TEC anomalies—Local TEC changes prior to earthquakes or TEC response to solar and geomagnetic activity changes? *Earth, Planets and Space*, *60*(9), 961–966. https://doi.org/10.1186/bf03352851

Afraimovich, E. L., Astafieva, E. I., & Kirushkin, V. V. (2006). Localization of the source of ionospheric disturbance generated during an earthquake. *International Journal of Geomagnetism and Aeronomy*, *6*(2). https://doi.org/10.1029/2004gi000092

Afraimovich, E. L., Perevalova, N. P., Plotnikov, A. V., & Uralov, A. M. (2001). The shock-acoustic waves generated by earthquakes. *Annales Geophysicae*, *19*(4), 395–409

Aki, K., & Richards, P. G. (2002). *Quantitative seismology*. University Science Books.

Ammon, C. J., Ji, C., Thio, H.-K., Robinson, D., Ni, S., Hjorleifsdottir, V., et al. (2005). Rupture process of the 2004 Sumatra–Andaman earthquake. *Science*, *308*(5725), 1133–1139. https://doi.org/10.1126/science.1112260

Artru, J., Ducic, V., Kanamori, H., Lognonné, P., & Murakami, M. (2005). Ionospheric detection of gravity waves induced by tsunamis. *Geophysical Journal International*, *160*(3), 840–848. https://doi.org/10.1111/j.1365-246x.2005.02552.x

Astafyeva, E. (2019). Ionospheric detection of natural hazards. *Reviews of Geophysics*, *57*(4), 1265–1288. https://doi.org/10.1029/2019RG000668

Astafyeva, E., & Heki, K. (2009). Dependence of waveform of near-field coseismic ionospheric disturbances on focal mechanisms. *Earth, Planets and Space*, *61*(7), 939–943. https://doi.org/10.1186/bf03353206

Astafyeva, E., Rolland, L. M., & Sladen, A. (2014). Strike-slip earthquakes can also be detected in the ionosphere. *Earth and Planetary Science Letters*, *405*, 180–193. https://doi.org/10.1016/j.epsl.2014.08.024

Azeem, I., & Barlage, M. (2018). Atmosphere–ionosphere coupling from convectively generated gravity waves. *Advances in Space Research*, *61*(7), 1931–1941. https://doi.org/10.1016/j.asr.2017.09.029

Bolt, B. A. (1964). Seismic air waves from the great 1964 Alaskan earthquake. *Nature*, *202*(4937), 1095–1096.

Borries, C., Jakowski, N., & Wilken, V. (2009). Storm induced large scale TIDs observed in GPS derived TEC. *Annales Geophysicae*, *27*(4), 1605–1612. https://doi.org/10.5194/angeo-27-1605-2009

Calais, E., Bernard Minster, J., Hofton, M., & Hedlin, M. (1998). Ionospheric signature of surface mine blasts from global positioning system measurements. *Geophysical Journal International*, *132*(1), 191–202.

Calais, E., & Minster, J. B. (1995). GPS detection of ionospheric perturbations following the January 17, 1994, Northridge earthquake. *Geophysical Research Letters*, *22*(9), 1045–1048.

Chang, L. C., Liu, J.-Y., & Palo, S. E. (2011). Propagating planetary wave coupling in SABER MLT temperatures and GPS TEC during the 2005/2006 austral summer. *Journal of Geophysical Research*, *116*(A10). https://doi.org/10.1029/2011JA016687

Dautermann, T., Calais, E., Lognonné, P., & Mattioli, G. S. (2009). Lithosphere–atmosphere–ionosphere coupling after the 2003 explosive eruption of the Soufriere Hills Volcano, Montserrat. *Geophysical Journal International*, *179*(3), 1537–1546. https://doi.org/10.1111/j.1365-246x.2009.04390.x

Davies, J. A., Lester, M., & Robinson, T. R. (1997). Deriving the normalised ion-neutral collision frequency from EISCAT observations. *Annales Geophysicae*, *15*(12), 1557–1569. https://doi.org/10.1007/s00585-997-1557-1

Davies, K., & Baker, D. M. (1965). Ionospheric effects observed around the time of the Alaskan earthquake of March 28, 1964. *Journal of Geophysical Research*, *70*(9), 2251–2253.

Donn, W. L., & Posmentier, E. S. (1964). Ground-coupled air waves from the great Alaskan earthquake. *Journal of Geophysical Research*, *69*(24), 5357–5361.

Drob, D. P., Emmert, J. T., Crowley, G., Picone, J. M., Shepherd, G. G., Skinner, W., et al. (2008). An empirical model of the Earth's horizontal wind fields: HWM07. *Journal of Geophysical Research*, *113*(A12). https://doi.org/10.1029/2008JA013668

Drob, D. P., Picone, J. M., & Garcés, M. (2003). Global morphology of infrasound propagation. *Journal of Geophysical Research*, *108*(D21). https://doi.org/10.1029/2002JD003307

Ducic, V., Artru, J., & Lognonné, P. (2003). Ionospheric remote sensing of the Denali Earthquake Rayleigh surface waves. *Geophysical Research Letters*, *30*(18). https://doi.org/10.1029/2003GL017812

Duputel, Z., Kanamori, H., Tsai, V. C., Rivera, L., Meng, L., Ampuero, J.-P., & Stock, J. M. (2012). The 2012 Sumatra great earthquake sequence. *Earth and Planetary Science Letters*, *351–352*, 247–257. https://doi.org/10.1016/j.epsl.2012.07.017

Gahalaut, V. K., & Catherine, J. K. (2006). Rupture characteristics of 28 March 2005 Sumatra earthquake from GPS measurements and its implication for tsunami generation. *Earth and Planetary Science Letters*, *249*(1–2), 39–46. https://doi.org/10.1016/j.epsl.2006.07.015

Hanks, T. C., & Kanamori, H. (1979). A moment magnitude scale. *Journal of Geophysical Research*, *84*(B5), 2348–2350. https://doi.org/10.1029/jb084ib05p02348

Heale, C. J., & Snively, J. B. (2015). Gravity wave propagation through a vertically and horizontally inhomogeneous background wind. *Journal of Geophysical Research: Atmospheres*, *120*, 5931–5950. https://doi.org/10.1002/2015JD023505

Heale, C. J., Snively, J. B., & Hickey, M. P. (2014). Numerical simulation of the long-range propagation of gravity wave packets at high latitudes. *Journal of Geophysical Research: Atmospheres*, *119*(19), 11116–11134. https://doi.org/10.1002/2014JD022099

Heki, K., & Ping, J. (2005). Directivity and apparent velocity of the coseismic ionospheric disturbances observed with a dense GPS array. *Earth and Planetary Science Letters*, *236*(3–4), 845–855. https://doi.org/10.1016/j.epsl.2005.06.010

Hill, E. M., Yue, H., Barbot, S., Lay, T., Tapponnier, P., Hermawan, I., et al. (2015). The 2012 Mw 8.6 Wharton Basin sequence: A cascade of great earthquakes generated by near-orthogonal, young, oceanic mantle faults. *Journal of Geophysical Research: Solid Earth*, *120*, 3723–3747. https://doi.org/10.1002/2014JB011703

Jones, R. M., & Bedard, A. J. (2018). Atmospheric gravity wave ray tracing: Ordinary and extraordinary waves. *Journal of Atmospheric and Solar-Terrestrial Physics*, *179*, 342–357. https://doi.org/10.1016/j.jastp.2018.08.014

Kiryushkin, V. V., & Afraimovich, E. L. (2007). Determining the parameters of ionospheric perturbation caused by earthquakes using the quasi-optimum algorithm of spatiotemporal processing of TEC measurements. *Earth, Planets and Space*, *59*(4), 267–278. https://doi.org/10.1186/bf03353104

Lay, E. H., Shao, X. M., Kendrick, A. K., & Carrano, C. S. (2015). Ionospheric acoustic and gravity waves associated with midlatitude thunderstorms. *Journal of Geophysical Research: Space Physics*, *120*(7), 6010–6020. https://doi.org/10.1002/2015JA021334

Lee, W. H. K., Lee, W. H. K., Lee, X., Munn, R. E., Stewart, S. W., & Stewart, S. W. (1981). Principles and applications of microearthquake networks (Vol. 2). Academic Press.

Le Pichon, A., Guilbert, J., Vega, A., Garcés, M., & Brachet, N. (2002). Ground-coupled air waves and diffracted infrasound from the Arequipa earthquake of June 23, 2001. *Geophysical Research Letters*, *29*(18), 33-1–33-4. https://doi.org/10.1029/2002GL015052

Liu, J.-Y., Tsai, Y.-B., Ma, K.-F., Chen, Y.-I., Tsai, H.-F., Lin, C.-H., et al. (2006). Ionospheric GPS total electron content (TEC) disturbances triggered by the 26 December 2004 Indian Ocean tsunami. *Journal of Geophysical Research*, *111*(A5). https://doi.org/10.1029/2005JA011200

Lognonné, P., Clévédé, E., & Kanamori, H. (1998). Computation of seismograms and atmospheric oscillations by normal-mode summation for a spherical earth model with realistic atmosphere. *Geophysical Journal International*, *135*(2), 388–406.

Mannucci, A. J., Iijima, B. A., Lindqwister, U. J., Pi, X., Sparks, L., & Wilson, B. D. (1999). *GPS and ionosphere, review of radio science 1996–1999*. URSI.

Manta, F., Occhipinti, G., Feng, L., & Hill, E. M. (2020). Rapid identification of tsunamigenic earthquakes using GNSS ionospheric sounding. *Scientific Reports*, *10*(1), 1–10. https://doi.org/10.1038/s41598-020-68097-w

McLoughlin, I. V., Wong, K. J., & Tan, S. L. (2011). Data collection, communications and processing in the Sumatran GPS array (SuGAr). In *Proceedings of the World Congress on Engineering* (Vol. 2, pp. 6–8).

McPherron, R. L., & O'Brien, P. (2001). Predicting geomagnetic activity: The D_{st} index. *Space Weather*, *125*, 339–345.

Medvedev, A. S., & Yiğit, E. (2019). Gravity waves in planetary atmospheres: Their effects and parameterization in global circulation models. *Atmosphere*, *10*(9), 531. https://doi.org/10.3390/atmos10090531

Meggs, R. W., Mitchell, C. N., & Spencer, P. S. (2004). A comparison of techniques for mapping total electron content over Europe using GPS signals. *Radio Science*, *39*(1). https://doi.org/10.1029/2002RS002846

Mikumo, T., & Watada, S. (2010). Acoustic-gravity waves from earthquake sources. In *Infrasound monitoring for atmospheric studies* (pp. 263–279). Springer.

Nayak, C., & Yiğit, E. (2018). GPS-TEC observation of gravity waves generated in the ionosphere during 21 August 2017 total solar eclipse. *Journal of Geophysical Research: Space Physics*, *123*, 725–738. https://doi.org/10.1002/2017JA024845

Occhipinti, G. (2016). The seismology of the planet Mongo: The 2015 ionospheric seismology review. Subduction dynamics: From mantle flow to mega disasters. *Geophysical Monographs*, *211*, 169–182.

Occhipinti, G., Lognonné, P., Kherani, E. A., & Hébert, H. (2006). Three-dimensional waveform modeling of ionospheric signature induced by the 2004 Sumatra tsunami. *Geophysical Research Letters*, *33*(20). https://doi.org/10.1029/2006GL026865

Occhipinti, G., Rolland, L., Lognonné, P., & Watada, S. (2013). From Sumatra 2004 to Tohoku-Oki 2011: The systematic GPS detection of the ionospheric signature induced by tsunamigenic earthquakes. *Journal of Geophysical Research: Space Physics*, *118*(6), 3626–3636. https://doi.org/10.1002/jgra.50322

Picone, J. M., Hedin, A. E., Drob, D. P., & Aikin, A. C. (2002). NRLMSISE-00 empirical model of the atmosphere: Statistical comparisons and scientific issues. *Journal of Geophysical Research*, *107*(A12), SIA–15. https://doi.org/10.1029/2002JA009430

ReVelle, D. O. (2008). Acoustic-gravity waves from bolide sources. *Earth, Moon, and Planets*, *102*(1–4), 345–356. https://doi.org/10.1007/s11038-007-9181-3

Rolland, L. M., Lognonné, P., Astafyeva, E., Kherani, E. A., Kobayashi, N., Mann, M., & Munekane, H. (2011a). The resonant response of the ionosphere imaged after the 2011 off the Pacific coast of Tohoku earthquake. *Earth, Planets and Space*, *63*(7), 853–857.

Rolland, L. M., Lognonné, P., & Munekane, H. (2011b). Detection and modeling of Rayleigh wave induced patterns in the ionosphere. *Journal of Geophysical Research*, *116*(A5). https://doi.org/10.1029/2010JA016060

Rolland, L. M., Occhipinti, G., Lognonné, P., & Loevenbruck, A. (2010). Ionospheric gravity waves detected offshore Hawaii after tsunamis. *Geophysical Research Letters*, *37*(17). https://doi.org/10.1029/2010GL044479

Rolland, L. M., Vergnolle, M., Nocquet, J.-M., Sladen, A., Dessa, J.-X., Tavakoli, F., et al. (2013). Discriminating the tectonic and non-tectonic contributions in the ionospheric signature of the 2011, Mw7.1, dip-slip Van earthquake, Eastern Turkey. *Geophysical Research Letters*, *40*, 2518–2522. https://doi.org/10.1002/grl.50544

Saito, A., Tsugawa, T., Otsuka, Y., Nishioka, M., Iyemori, T., Matsumura, M., et al. (2011). Acoustic resonance and plasma depletion detected by GPS total electron content observation after the 2011 off the Pacific coast of Tohoku earthquake. *Earth, Planets and Space*, *63*(7), 863–867. https://doi.org/10.5047/eps.2011.06.034

Subarya, C., Chlieh, M., Prawirodirdjo, L., Avouac, J.-P., Bock, Y., Sieh, K., et al. (2006). Plate-boundary deformation associated with the great Sumatra–Andaman earthquake. *Nature*, *440*(7080), 46–51. https://doi.org/10.1038/nature04522

Sunil, A. S., Bagiya, M. S., Reddy, C. D., Kumar, M., & Ramesh, D. S. (2015). Post-seismic ionospheric response to the 11 April 2012 East Indian Ocean doublet earthquake. *Earth, Planets and Space*, *67*(1), 1–12. https://doi.org/10.1186/s40623-015-0200-8

Suzuki, S., Shiokawa, K., Otsuka, Y., Kawamura, S., & Murayama, Y. (2013). Evidence of gravity wave ducting in the mesopause region from airglow network observations. *Geophysical Research Letters*, *40*, 601–605. https://doi.org/10.1029/2012GL054605

Suzuki, S., Vadas, S. L., Shiokawa, K., Otsuka, Y., Kawamura, S., & Murayama, Y. (2013). Typhoon-induced concentric airglow structures in the mesopause region. *Geophysical Research Letters*, *40*, 5983–5987. https://doi.org/10.1002/2013GL058087

Torrence, C., & Compo, G. P. (1998). A practical guide to wavelet analysis. *Bulletin of the American Meteorological Society*, *79*(1), 61–78. https://doi.org/10.1175/1520-0477(1998)079<0061:apgtwa>2.0.co;2

Tsai, H.-F., Liu, J.-Y., Lin, C.-H., & Chen, C.-H. (2011). Tracking the epicenter and the tsunami origin with GPS ionosphere observation. *Earth, Planets and Space*, *63*(7), 63. https://doi.org/10.5047/eps.2011.06.024

Warnant, R., & Pottiaux, E. (2000). The increase of the ionospheric activity as measured by GPS. *Earth, Planets and Space*, *52*(11), 1055–1060. https://doi.org/10.1186/bf03352330

Yadav, R. K., Kundu, B., Gahalaut, K., Catherine, J., Gahalaut, V. K., Ambikapthy, A., & Naidu, M. S. (2013). Coseismic offsets due to the 11 April 2012 Indian Ocean earthquakes (Mw8.6 and 8.2) derived from GPS measurements. *Geophysical Research Letters*, *40*, 3389–3393. https://doi.org/10.1002/grl.50601

Yeh, K. C., & Liu, C. H. (1974). Acoustic-gravity waves in the upper atmosphere. *Reviews of Geophysics*, *12*(2), 193–216. https://doi.org/10.1029/rg012i002p00193

Young, J. M., & Greene, G. E. (1982). Anomalous infrasound generated by the Alaskan earthquake of 28 March 1964. *Journal of the Acoustical Society of America*, *71*(2), 334–339. https://doi.org/10.1121/1.387457

Yu, Y., & Hickey, M. P. (2007). Time-resolved ducting of atmospheric acoustic-gravity waves by analysis of the vertical energy flux. *Geophysical Research Letters*, *34*(2). https://doi.org/10.1029/2006GL028299

Yue, H., Lay, T., & Koper, K. D. (2012). En échelon and orthogonal fault ruptures of the 11 April 2012 great intraplate earthquakes. *Nature*, *490*(7419), 245–249. https://doi.org/10.1038/nature11492

Zhong, J., Lei, J., Dou, X., & Yue, X. (2016). Assessment of vertical TEC mapping functions for space-based GNSS observations. *GPS Solutions*, *20*(3), 353–362. https://doi.org/10.1007/s10291-015-0444-6